ICAS 2021 SHANGHAI
International Council of the Aeronautical Sciences
32nd Congress of the International Council of the Aeronautical Sciences
September 6-10, 2021
Pudong Shangri-La, Shanghai, China

Study on the Heat Flux of Hypersonic Shock Wave Boundary Layer Interaction Controlled by a Micro-Ramp Vortex Generator

Dong Sun[1], Chen Li[1], Hengyu Cai[2], Qilong Guo[1], Pengxin Liu[1]* & Xianxu Yuan[1]

1 State Key Laboratory of Aerodynamics. Mianyang Sichuan 621000, China;

2 School of Aeronautics, Northwestern Polytechnical University, Xi'an, Shaanxi 710072, China

Abstract

A direct numerical simulation at Mach 5 is performed to investigate the effects of the micro-ramp vortex generator on the heat flux after the hypersonic shock wave/boundary layer interaction. The vortical structures in the wake flow the downstream of micro-ramp vortex generator are analyzed. The scaling laws for the wake flow are tested. It is found the scaling laws, which were first proposed for the supersonic flow, can also be used in the hypersonic flow with some modification about the effects of the trailing-edge shocks. We further investigated the unsteadiness of the heat flux in the wake flow. The heat flux in the centerline is reduced by the wake flow effectively. However, the wake flow will cause remarkable non-uniformity of the heat flux. And the most energy-containing frequency is 0.4~0.5 U_∞/δ. The dynamic mode decomposition was performed to analyze the spatial modes of the heat flux. The spanwise stripes in the case with MVG were observed which may serve as evidence of the interaction of the arc-like vortices and the separation shock waves.

Keywords: Micro-ramp vortex generator; Shock wave/boundary layer interaction; hypersonic; Direct numerical simulation

1. Introduction

In the design of hypersonic aircraft, shock wave/boundary layer interaction (SWBLI) must be considered carefully, because it usually causes adverse pressure gradient and unsteady bubble that leads to strong unsteadiness and local extreme heating. Hence, some devices must be employed to alleviate these adverse effects.

The micro-ramp vortex generator (MVG) has been extensively adopted in the supersonic SWBLI to control the unsteady separation. The height of MVG is usually 0.2~0.5 times the thickness of the local boundary layer, which may not result in a notable drag increase and the streamwise vortices generated at the two sides can reduce the size of separation effectively. The current study on the supersonic MVG focuses on two aspects, i.e., (1) the optimization of MVG and (2) the detailed mechanism of flow control.

On the optimization of MVG, Anderson optimized the shape of MVG by response surface methods and applied the optimized MVG in the control of oblique shock wave boundary interaction. Babinsky adopted the optimized MVG in his series experiments to study the flow structures and the optimal height and mounting position of MVG. In his experiments, he revealed the detailed shock structures and the vortical structures around MVG. He further found that the flow structures can be scaled geometrically with device height and the smaller MVGs are recommended. Giepman[2] investigated the effects of the height and the mounting position of MVG. He found the higher MVG have better performance in reduce the separation size and no MVG can remove the separation completely. The main effect of MVG is the modulation of the separation size in the spanwise direction. Ghosh[3] obtained similar results in his hybrid RANS/LES combined with immersed boundary methods and found that MVG would elongate the separation at the centerline and shorten the region in the spanwise direction.

On the control mechanism of MVG, the vortical structures induced by MVG attract the most attention. Babinsky identified a pair of primary streamwise vortices and multiple secondary vortices in the wake flow of MVG. And above the wake, the unsteady arc-like vortices were observed[4]. Li and Liu[4] revealed that the arc-like vortices were caused by the Kelvin-Helmholtz (K-H) shear

layer instability. Lu's experiment further proved their deduction. With help of tomographic PIV, Sun measured the arc-like vortices[4] and investigated the decaying process of wake flow. He proposed scaling laws for the time-averaged velocity and turbulent fluctuations. More studies about the vortical structures and mechanism of MVG can refer to the reviews of Lin[6], Lu[7] and Panaras[8].

Concerning the hypersonic SWBLI, the studies on the control effects of MVG are rare. In the hypersonic flow, compressibility plays a more significant role as the Mach number increases. Besides the unsteady separation bubble, the SWBLI in the hypersonic flow also leads to a local peak of heat flux, which is much higher than that on the flat plate. Our previous work has shown that MVG has great potential in controlling the local heat flux induced by SWBLI[9]. In this paper, we continued performing a direct numerical simulation of hypersonic SWBLI at Mach 5 to study the unsteadiness of heat flux of SWBLI controlled by MVG.

The work of this paper is organized as follows. Section 2 describes the numerical methods and geometry of MVG in brief. Section 3 presents the vortical structures around the MVG and the scaling laws for the time-averaged velocity. In section 4, the statistical parameters and modal analysis on the unsteadiness of the heat flux are given. Finally, in section 5, some conclusions are drawn.

2. Governing Equations and Computational Setup

The compressible non-dimensional Navier-Stokes conservation equations in the curvilinear coordinate form are employed in the present simulation. The two-dimensional sketch of the computation domain is presented in Figure 1. The angle of the compression corner is 24 degree. The streamwise length before the corner is set as L_{x1}=503 which are normalized by the momentum thickness at the inlet. The lengths used in the rest of the paper are all normalized by θ_{in} without extra specification. The streamwise length after the corner is set as L_{x2}=170.5. The height of the domain is L_y=77.8. The width is L_z=41.0 which is not shown in the Figure. The MVG is mounted at X_{MVG}=320.4 downstream of the inlet. The geometric parameters of MVG are h=4.65，α=8.64°，β=70°，γ=24°，C=7.2h. The distribution of grid points on the MVG is given in Fig. 2(b). The grids points are generally smoothly distributed and the orthogonality at the wall is good except for some singularities at the edges of the MVG. The number of grid points to discretize the domain is $N_x \times N_y \times N_z = 2331 \times 181 \times 301$. At the inlet, the spanwise grid spacing in wall units is dz^+=4.2, the streamwise grid spacing is dx^+=5.92 and the normal grid spacing at the first point off the wall is dy^+=0.46. The spacing is believed small enough for direct numerical simulation compared with the DNS simulations in the references. The SWBLI without MVG is also simulated with the same configuration size, discretization methods and inflow conditions with the case with MVG. The grid number for the case without MVG is $\mathrm{N_x} \times \mathrm{N_y} \times \mathrm{N_z} = 2195 \times 181 \times 301$.

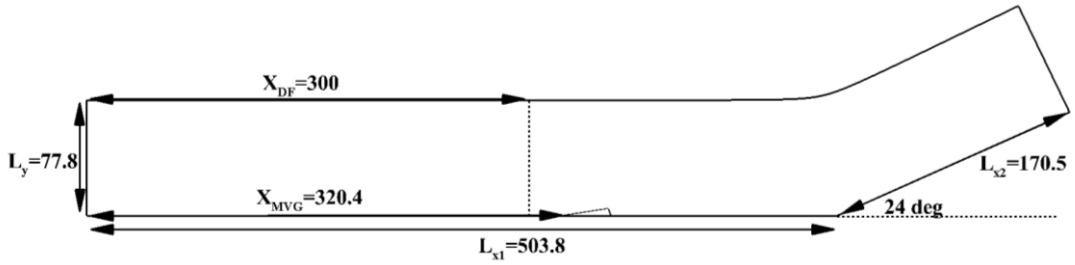

Figure 1 The sketch of the computational domain

A hybrid finite difference scheme is applied to discretize the inviscid flux by the Ducros shock sensor[11]. The Ducros sensor is given by

$$\Phi = \frac{(\nabla \cdot \vec{u})^2}{(\nabla \cdot \vec{u})^2 + (\nabla \times \vec{u})^2 + \varepsilon}$$

where ε is specified as 10^{-3} in the present work. When Φ is greater than a threshold value which is 0.01 in our simulation, the seventh-order WENO scheme[12] is used, otherwise the eighth-order skew-symmetry scheme[13] is employed. For the discretization of the viscous flux, the eighth-order central scheme is used. The DPLUR dual-step method[14] is adopted as the temporal

algorithm. The time step *dt* is $0.01\,\theta_{in}/u_{\infty}$.

The van Driest transformed velocity $U_{VD}^{+} = \int_0^{u^+} (\rho/\rho_w)^{0.5} du^+$ showed good agreement with the log-law in Figure 2(a). The Reynolds stresses normalized by the wall density and friction velocity $R_{ij}/u_\tau^2 = \overline{\rho u'_\iota u'_j}/\overline{\rho_w}\,u_\tau^2$ was presented in Figure 2(b). The DNS results by Pirozzoli and experimental results by Elena about the supersonic turbulent boundary layer were adopted as a comparison. The results in Figure 2 showed that the digital filter method could produce a turbulent boundary layer with good mean and statistical properties.

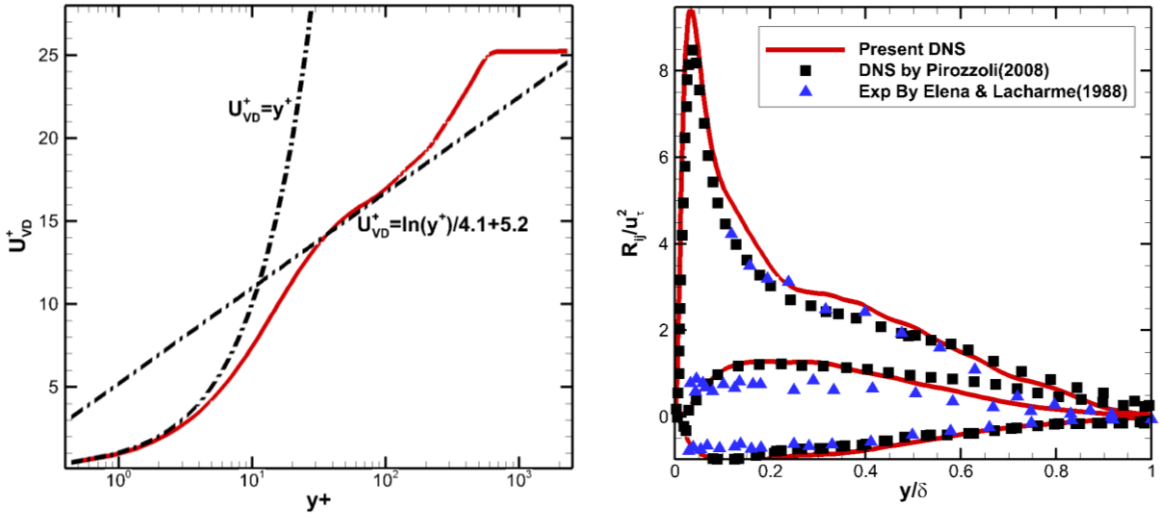

Figure 2 The turbulent mean velocity and Reynolds stresses profiles at XMVG，(a) van driest transformed mean streamwise velocity, (b) Reynolds stresses normalized by friction velocity and density at the wall

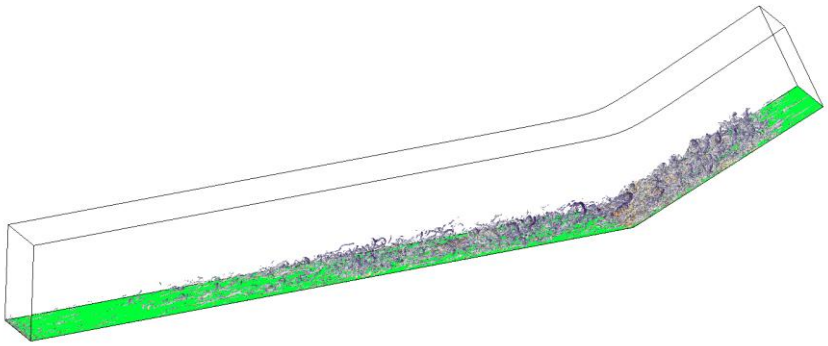

Figure 3 The instantaneous vortical structures displayed by Q criterion coloured by streamwise velocity

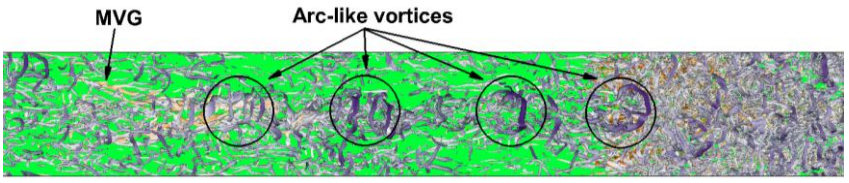

Figure 4 The arc-like vortical structures around MVG

3. Flow Structures Around Micro-ramp Vortex Generator

The instantaneous vortical structures displayed by *Q* criterion[15] are presented in Figure 3. The Q criterion which can be expressed as,

$$Q_{cr} = \frac{1}{2}(|S|^2 - |\Omega|^2)$$

has been employed to identify the vortices extensively. The threshold value was adjusted to 0.01 to display the arc-like vortices in the wake of MVG. However, the vortical structures in the upstream turbulent boundary layer cannot be presented at this threshold value, which suggested that the intensity of the wake structures is much stronger than that of the upstream boundary layer. In Figure 4, a zoomed picture is presented. The arc-like vortices can be clearly observed downstream of MVG. The arc-like vortices will experience four stages. In the beginning, the arc-like vortices are generated on the upper side of two primary streamwise vortices due to Kelvin-Helmholtz (K-H) shear layer instability[4]. The shape of the streamwise and arc-like vortices seems regular. After entering the nonlinear stage, the size of the arc-like vortices will grow quickly and the primary streamwise vortices will be affected. At the third stage, the streamwise vortices have been destroyed by the oversized arc-like vortices. And it can be observed that not all of the upstream arc-like vortices can survive at this stage. Some of them went into the lateral turbulent flow and their intensity decrease quickly. At the last stage, the arc-like vortices will impinge on the separation shock wave.

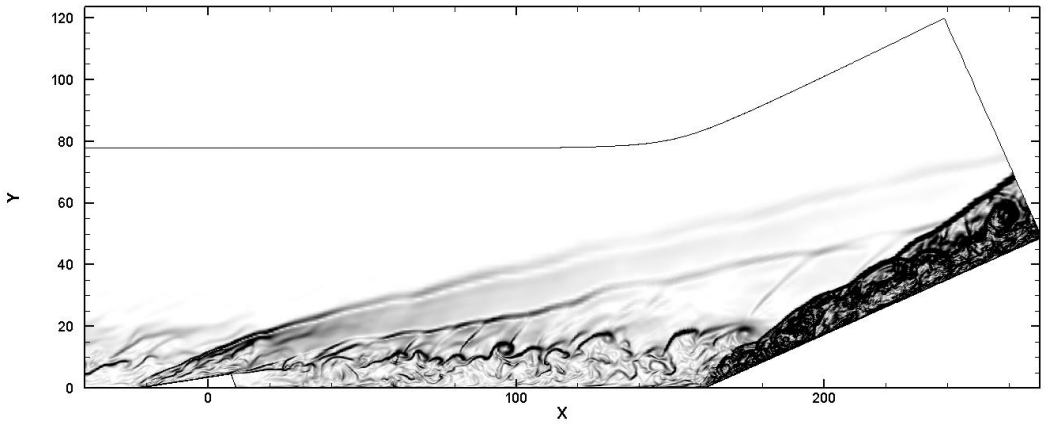

Figure 5 the contours of the instantaneous density gradient magnitude at the centre plane.

In Figure 5, the instantaneous density gradient magnitude was displayed to demonstrate the shock wave system in the MVG wake flow. Two shocks at the leading- and trailing edge of the MVG can be observed which are consistent with the experiment of Babinsky. In the wake, some Mach waves can be found between the arc-like vortices and trailing-edge shock. These Mach waves were generated by the supersonic flow past the arc-like vortices, which are not observed in supersonic cases.

4. Impact of Micro-ramp Vortex Generator on Separation and Heat Flux

After the investigation of the mean properties of momentum deficit, in this section, we will focus on its impact on the pressure and heat flux in the interaction zone. The time-averaged wall pressure was presented in Figure 6. The distributions are similar in both cases except for two minor differences. The first difference is after the trailing edge of the MVG, the pressure decreased because of the expansion effect. The second difference is the low-pressure zone after the interaction zone which was induced by the primary streamwise vortices. In the previous section, we found the primary streamwise vortices were affected the arc-like vortices and broke up into smaller vortices. However, the contours of mean pressure revealed that the impact of primary vortices can persist a very long distance. The contours of the time-averaged heat flux Q_w ($Q_w = q_w/0.5\rho_\infty U_\infty^3$) are presented in Figure 7. Unlike the mean pressure, the contours of heat flux displayed significant differences between the two cases. First, the MVG would not result in very high heat flux. This is probably thanks to the height of the MVG, only about 25 per cent of the local boundary layer thickness. Two streaks with high heat flux can be found after the trailing edge of MVG, which were caused by the reattachment of vortices at two sides of MVG. Second, both streaks would decay quickly in a short distance corresponding to the destruction of the primary vortices. Third, as reported in our previous paper[9], the heat flux at the centerline of the interaction became quite low compared with the case without MVG. This result indicated that the primary streamwise vortices

can reduce the heat flux peak of the SBLI effectively. However, the heat flux at the two sides of the interaction zone increased because of the reattachment of the vortices.

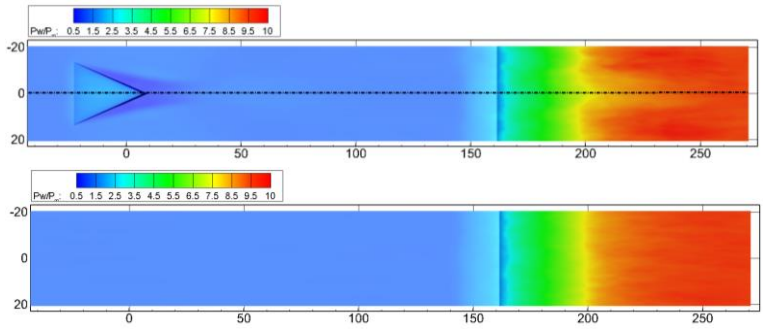

Figure 6 The time-averaged pressure on the wall. The upper is the case with MVG and the lower is the case without MVG

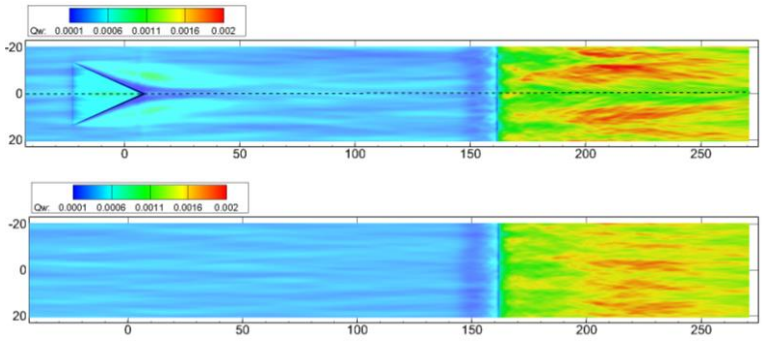

Figure 7 The time-averaged heat flux on the wall the upper is the case with MVG and the lower is the case without MVG

To investigate the heat flux distribution in the interaction zone, the distributions of the time and spanwise averaged pressure and heat flux were given in Figure 8 and Figure 9, respectively. The distributions of both cases are similar. The pressure and the heat flux at the interaction zone were not augmented by MVG apparently. It should be noted that the difference in length of the interaction zone in the two cases was not obvious, which indicate that the effect of MVG on the separation is not significant. Two reasons can be employed to interpret this. First, a small corner angle in hypersonic flow caused a small separation zone. Meanwhile, no significant alteration of the separation appears due to the rather small size of MVG. The distributions of the pressure and the heat flux at the centerline were added in Figure 8 and Figure 9 to show the impact of primary streamwise vortices. The pressure in the interaction zone was slightly lower than the spanwise averaged one. In the interaction zone, the heat flux at the centerline was greatly suppressed by MVG, which can be observed in Figure 9. The heat flux at the centerline reached the peak value (about 4.5 times heat flux in the incoming boundary layer Q_{BL}) at the reattachment and decreased to $3.6Q_{BL}$ continuously. The spanwise averaged heat flux reached its peak downstream of the interaction and the peak value is about $5.0Q_{BL}$. The results showed that the primary streamwise vortices altered the separation structures in the interaction zone[9].

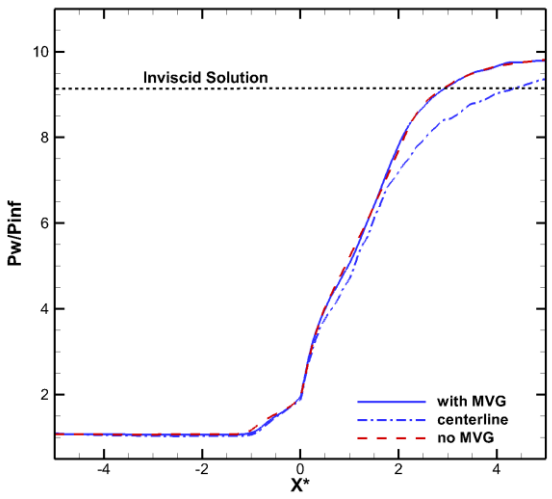

Figure 8 the time and spanwise averaged wall pressure

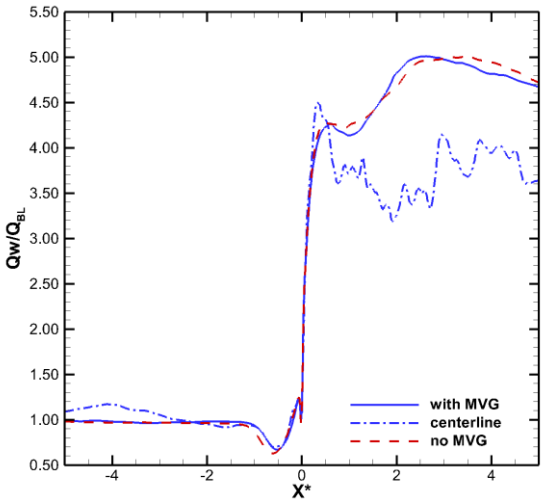

Figure 9 The time and spanwise averaged wall heat flux

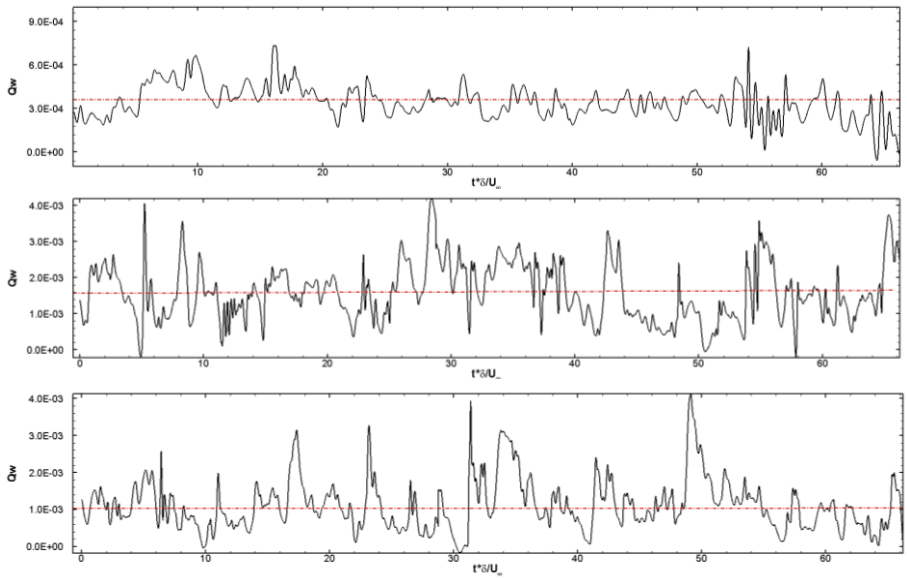

Figure 10 The heat flux signals at multiple streamwise locations.

Table 1 The statistical parameters of P1-P3

	P1	P2	P3
Mean Value	3.4E-4	1.6E-3	1.1E-3
Standard Deviation	8.8E-5	6.3E-4	5.2E-4
Skewness	0.17	0.48	1.18

After the discussion of the time-averaged properties of the heat flux, the unsteadiness should be investigated. The signals of the heat flux at multiple streamwise locations, i.e., P1, P2 and P3 are presented in Figure 10. The position of P1 is at the upstream boundary layer, the position of P3 is at the centre of the interaction zone and the position of P2 is at the left side of P3 where the heat flux is greater than that of P3 due to the reattachment of the primary vortices. The sampling frequency is $5.0U_\infty/\theta_{in}$ and the total number of samples is 5962. Although the time-averaged heat flux at P3 is much lower than that at P2, at some instant, the heat flux at P3 reached the maximum of the heat flux at P2. The statistical parameters, i.e., mean value, standard deviation and skewness of P1-P3 were given in Table 1. The skewness in Table 1 indicated that the symmetry of the probability distribution functions (PDF) of P1, P2 and P3 were different. The PDF of P1 is nearly symmetry while the PDFs of P2 and P3 were not. The results indicate that the MVG can

alleviate the time-averaged heat flux after the interaction, but the wake flow will cause remarkable non-uniformity of the heat flux.

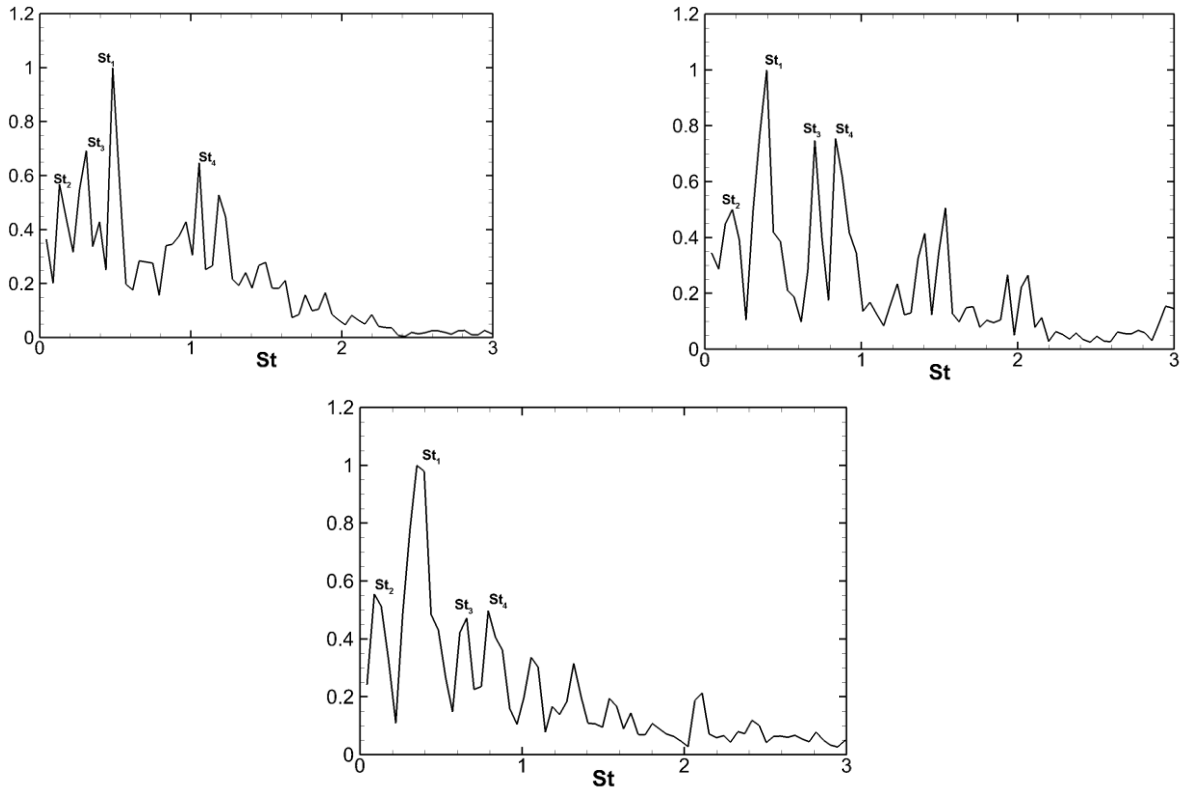

Figure 11 the weighted power spectral of heat flux at multiple streamwise locations

The pre-multiplied power spectral densities of P1-P3 were obtained and presented in Figure 11. The non-dimensional frequency *St* is defined as $St = f\delta/U_\infty$. Because of the total sampling length, the frequency lower than *St*=0.05 cannot be detected. At P1, the upstream boundary layer, the heat flux has most of its energy at the St_1=0.48 and has some energy at St_2=0.12, St_2=0.30 and St_4=1.05. The frequency St_4 is the characteristic frequency of the present turbulent boundary layer which is not evident in the power spectra of the heat flux in the interaction zone, i.e., P2 and P3. However, the most energy-containing frequency is about St_1=0.4, which is slightly smaller than that at P1. There are two peaks between the St_1=0.4 and *St*=1.0, whose value are 0.66 and 0.82. Moreover, it should be noted that these two peaks exist in higher frequency at P2. In a summary, the most energy-containing frequency is about *St*=0.4~0.5, which is apparently higher than the frequency of the shock motion ($0.01\sim0.001\,U_\infty/\delta$). Therefore, the reason for the heat flux is complicated and related to the impinging of the vortices with medium frequencies.

5. Dynamic mode decomposition

To further investigate the heat flux, the dynamic mode decomposition (DMD) has been performed. Compared with the usual proper orthogonal decomposition (POD), DMD can obtain the frequency and growth rate for each spatial mode. We performed DMD with 800 samples and the interval of samples is $0.1\delta/U_\infty$. The real and imaginary part of the eigenvalues is scattered in Fig. 11. The real parts denote the growth rate of the DMD modes and the imaginary denote the angular frequency. In Fig. 11, all the real parts of the eigenvalues of both cases are negative which indicate all the modes are nearly stable in time. In Fig. 12, the magnitude and frequency *St* are presented. *St* is defined as $St=f\delta/U_\infty$. Six modes with the greatest magnitude are labelled as M0-M5 in Fig. 13. The M0 is the mode with zero-frequency which denotes the time-averaged field. In the case without MVG,

the frequencies of these modes located in the range of St=0.01~0.05, while in the case with MVG, the energy-contained frequencies located in the range of St=0.1~0.3 which is much higher than those in the case without MVG. The reason for this difference may be the interaction of the arc-like vortices and the separation shock. To prove this deduction, the spatial distributions of the DMD modes are presented in Fig. 14 and Fig. 15.

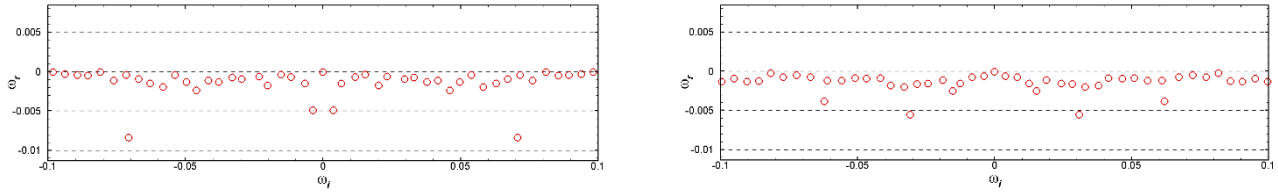

(a) (b)

Fig. 12 DMD logarithmical eigenvalue mapped to the complex plane (a: the case without MVG and b: the case with MVG)

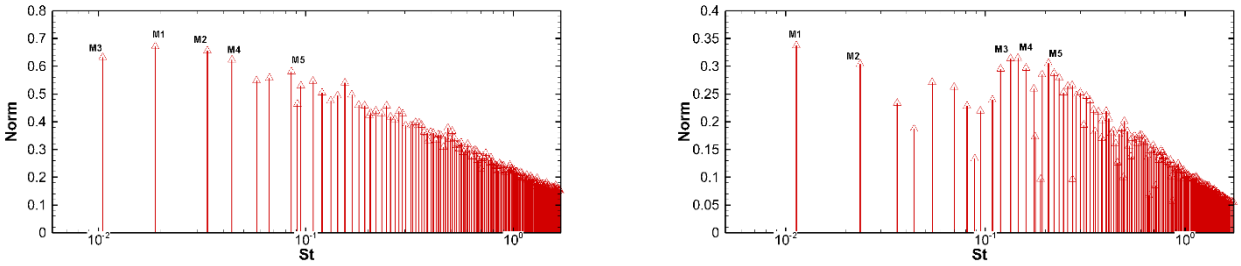

(a) (b)

Fig. 13 Relationship between the DMD modes and the frequencies (a: no MVG, b: MVG)

The distributions of M0 are similar to those in Fig. 7. For the M1, the streamwise stripes can be observed in both cases and a higher magnitude is observed in the case without MVG. For the M2, distinct differences occurred. In the case without MVG, the streamwise stripes are still dominant while in the case with MVG, the positive and negative stripes along the spanwise direction appear. These spanwise stripes can be still observed in M3, M4 and M5. The impingements of the arc-like vortices are probably the cause of these stripes. As the streamwise distance increase, the strength of the arc-like vortices will get stronger and the size will get bigger. After they will interact with the separation shock wave and the wave structures nearby will be affected. The stripes are the footprint of these interactions.

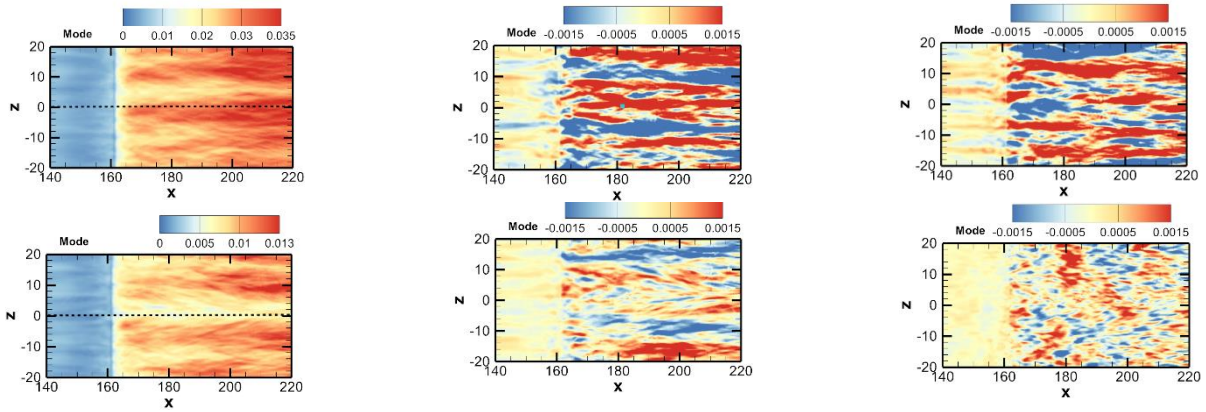

Fig. 14 Spatial distribution of real part of DMD mode (from up to right: mode0, mode1 and mode2, the upper row is the case without MVG and the lower row is the case with MVG)

6. Conclusion and Summary

A direct numerical simulation is performed on the SWBLI at Mach 5 with the control of a micro-ramp vortex generator. The development of the arc-like vortices in the wake flow of the MVG is analyzed. We further analyze the heat flux after the SWBLI and found that the heat flux at the centerline of MVG is lower than the two sides. The most energy-containing frequency is 0.4~0.5U_∞/δ which is related to the impinging vortices. We further prove this deduction by dynamic mode decomposition. The positive and negative stripes in the spatial distribution of the dynamic modes may be caused by the interaction of the arc-like vortices and the separation shocks.

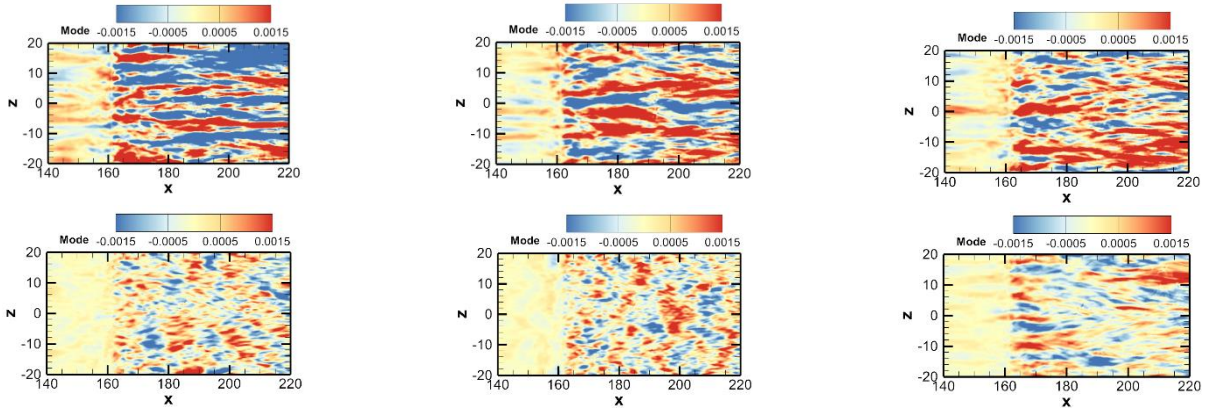

Fig. 15 Spatial distribution of real part of DMD mode (from up to right: mode3, mode4 and mode5, the left is the case with MVG and the right is the case without MVG)

7. Contact Author Email Address

Corresponding author: liupengxin@cardc.cn

8. Copyright Statement

The authors hold copyright on all of the material included in this paper and confirm that they give permission for the publication and distribution of this paper as part of the ICAS proceedings or as individual off-prints from the proceedings.

Acknowledgements

This work is supported by the (2019YFA0405300), National Natural Science Foundation of China (11802324) and National Numerical Windtunnel project.

References

[1] Anderson B. H., Tinapple J., Surber L, Optimal Control of Shock Wave Turbulent Boundary Layer Interactions Using Micro-Array Actuation, AIAA Paper 2006-3197.

[2] Giepman R. H., J. Schrijer, and B. W. Oudheusden, “Flow control of an oblique shock wave reflection with micro-ramp vortex generators: Effects of location and size,” Phys. Fluids 226, 066101 (2014).

[3] Ghosh S., Choi J. I., and Edwards J. R., “Numerical simulations of effects of micro vortex generators using immersed-boundary methods,” AIAA J. 48(1), 92–103 (2010)

[4] Sun Z., F. Schrijer F. J., Scarano F., and van Oudheusden B. W., “The threedimensional flow organization past a micro-ramp in a supersonic boundary layer,” Phys. Fluids 24, 055105 (2012)

[5] Li Q. and Liu C., “Implicit LES for supersonic micro-ramp vortex generator: New discoveries and new mechanisms,” Modell. Simul. Eng. 2011, 1.

[6] Lin, J.C., Review of research on low-profile vortex generators to control boundary-layer separation. Prog.Aerosp.Sci., 2002. 38(4-5): p. 389-420.

[7] Lu, F., Q. Li, and C. Liu, Micro-vortex generators in high-speed flow. Prog.Aerosp.Sci., 2012. 53:

p. 30-45.

[8] Panaras, A.G. and F.K. Lu, Micro-vortex generators for shock wave/boundary layer interactions. Prog.Aerosp.Sci., 2015. 74: p. 16-47.

[9] D. Sun, Q. Guo, C. Li, and P. Liu, “Direct numerical simulation of effects of a micro-ramp on a hypersonic shock wave/boundary layer interaction,” Phys. Fluids 31, 126101 (2019).

[10] D. Sun, Chen J, Li C., Liu P, Guo Q, Yuan X, On the wake structure of a micro-ramp vortex generator in hypersonic flow, Phys. Fluids 32, 126111 (2020).

[11] Ducros F., Ferrand V., Nicoud F., Weber C., and Darracq F., Large-eddy simulation of the shock/turbulence interaction, J. Comput. Phys. 152, 517–549 (1999).

[12] Shu C. W., Essentially non-oscillatory and weighted essentially non-oscillatory schemes for hyperbolic conservation laws, NASA/CR-97-206253, ICASE Report No. 97-65, 1997.

[13] Pirozzoli S., Generalized conservative approximations of split convective derivative operators, J. Comput. Phys. 229, 7180–7190 (2010).

[14] Martín M. P. and Candler G. V., A parallel implicit method for the direct numerical simulation of wall-bounded compressible turbulence, J. Comput. Phys. 215, 153–171 (2006).

[15] Hunt J., Wray A., and Moin P., Eddies, streams, and convergence zones in turbulent flows, in Proceedings of the 1988 Summer Program of the Center for Turbulence Research, 1988.